The unusual size effect of eutectic Sn/Pb alloys in the micro regime: experiments and modeling

K. F. Gan, A.H.W.Ngan*

Department of Mechanical Engineering, The University of Hong Kong, Pokfulam Road, Hong Kong, People's Republic of China

* Corresponding author (email: hwngan@hku.hk)

Abstract

Eutectic alloys are widely used as solder-joint materials due to their suppressed melting points, but when used in micro-devices with small dimensions, their characteristic lamellar microstructure may lead to an internal length scale that affects strength. Here, we report an unusual 'smaller-being-weaker' phenomenon in eutectic Sn/Pb alloys with fine lamellar microstructure, namely, in the specimen-size regime close to and slightly larger than the interphase lamellar spacing, the strength decreases with decreasing size, while above this regime the strength tends towards the bulk value. Theoretical modeling indicates that in a fine lamellar microstructure, high contents of dislocations are retained, so that strength is governed by mutual dislocation interactions, rather than by dislocation starvation. Therefore, in smaller samples, fewer interphase lamellar boundaries are present to block dislocations, thus resulting in a 'smaller-being-weaker' behavior. In samples a lot larger than the lamellar spacing, significant strengthening arises from Taylor hardening and mutual dislocation interactions as a result of significant dislocation retention by the interphase boundaries, so that strength does not depend on specimen size anymore. In a course lamellar microstructure, however, even a larger micro-specimen may contain insufficient interphase boundaries to significantly retain dislocations, and strength may be governed by the starvation effect due to significant loss of dislocations at free surfaces. In this case, the size effect of strength

may become a lot milder, or even exhibit the conventional "smaller-being-stronger" behavior. The results here supplement conventional knowledge on size effects in micro-scaled crystalline materials, and provide important implications on solder-joint design in micro-devices.

***Keywords*:** size effect; eutectic; lamellae; micropillars; dislocation.

1. Introduction

In the last decade, size effects of micro-scaled metallic materials have been intensively investigated [1-3], and a 'smaller-being-stronger' phenomenon, reported for the first time in metallic whiskers in the 1950's [4], has now been established as the norm behavior of monolithic metals of micro sizes. Such a deformation behavior obeys a power law of size [5-8] and has a jerky, stochastic nature [9-11]. In small crystals, mobile dislocations can glide to and annihilate freely at free surfaces without significant accumulation or multiplication, leading to a sustained dislocation-starved state with a high flow stress [3, 12], and the quantized emission of new dislocations to maintain the plastic flow leads to discrete strain bursts of a stochastic nature [10, 13]. In larger, but still micro-sized, crystals, a 'source truncation' mechanism operates in which single-armed dislocation sources truncated by free surfaces govern the flow stress, and since the source arms in smaller specimens are generally shorter, their operational stress and hence the flow stress is higher [14-16]. As the loss of dislocations is the cause for the strain bursts and jerky deformation [9, 13, 17-19], to improve the deformation behavior a number of attempts have been made to control the dislocation density in micro specimens, via means including pre-straining [13, 20, 21], surface coating [21, 22], inserting grain boundaries [23-25]. In fact, the majority of real-life metallic materials for engineering applications are alloys with complicated microstructures, such as second-phase precipitates, grains, inclusion particles, twins or solutes. Hence, understanding the size effect of metals with merely a monolithic, single-crystalline structure would be insufficient and indeed irrelevant for real applications, and for alloys in real use their complicated microstructures should introduce an internal scale length that would couple with the external specimen size to affect the mechanical behavior [26-30]. For example, an unusual phenomenon of a "weakest size" in the micro-regime was recently discovered in duralumin with a precipitated microstructure, due to the

interplay between the dislocation-starvation mechanism controlled by the external sample size in the micro range, and the precipitation-hardening mechanism controlled by the internal length scale of the precipitate spacing [31].

Eutectic Sn/Pb solders have been widely used for electrical and structural joints due to their low melting points, good wettability, acceptable electrical conductivity and good plasticity [32-35]. The typical microstructure of eutectic Sn/Pb alloys features alternant lamellae of the two constituent phases with an average spacing that is sensitive to the solidification conditions of the alloy [36, 37]. Recently, the length-scale dependent plasticity in metallic multilayers fabricated by successive physical deposition has been studied [38-40], and the results also conform to the "smaller-being-stronger" rule in that strength monotonically increases as the multilayer thickness decreases. In lamellar Ti-Al alloys in which the lamellae are formed naturally in the wrought process, the lamellar spacing rather than the grain size dominates the yield strength according to a dependence similar to the Hell-Patch relation [41]. However, the notion of "smaller-being-stronger" for lamellar materials has been challenged by the observation that the finer lamellar microstructure leads to lower tensile flow strength in cast Al-based alloys [42]. In summary, although the plasticity of small-size materials coupled with multiple length scales of the internal microstructures has received a lot of attention [43-46], understanding on how the strength of micro-sized eutectic alloys depends on their lamellar layers is still lacking.

In this article, we report a significant 'smaller-being-weaker' size effect of strength in micro-sized eutectic Sn/Pb alloys with a characteristic lamellar microstructure. By controlling the lamellar spacing through different solidification treatments, the effect of the internal length scale on the deformation behavior of Sn/Pb micropillars is studied. Theoretical modeling based on a

continuum dislocation model and two-dimensional dislocation dynamics simulations is carried out to understand the reason of such an unusual size effect of strength.

2. Experimental

An as-received eutectic Sn/Pb alloy (63 wt. % Sn-37 wt. % Pb) was used as the starting material. A large piece of the specimen was cut into two which were then melted by heating over the eutectic point of 183℃. Afterwards, one piece of the specimen was air cooled (AC) at room temperature (RT ~ 20℃), whilst the other was slowly cooled within the furnace (FC). The oxide layers of the sample surfaces were removed by mechanical polishing. The samples were then left to fully age at RT for more than two weeks to achieve a stable microstructure [33]. Then, the AC and FC samples were mechanically ground and fine-polished with 1 μm diamond paste to achieve mirror-like surfaces. They were then further vibration-polished with a Buehler VibroMet 2 polisher using a MasterSet 0.06 μm colloidal silica suspension with anhydrous alcohol to achieve a stress-free surface state.

The eutectic microstructure of the samples was examined using a Hitachi S4800 FEG scanning electron microscopy (SEM). Micropillars were milled using focused ion-beam (FIB) milling by an FEI Helios Nanolab 600i dual beam FIB/SEM system operated at 30 kV ion beam voltage. Since both the AC and FC samples were cut from the same as-received alloy and melted and cast in the same way albeit cooled differently after reheating to above the eutectic temperature, they contained large grains oriented close to the ~[001] direction. Thus, in both the AC and FC samples, a large grain with an orientation ~ [001] and size larger than 500 μm, as detected by electron backscattered diffraction (EBSD), was selected for milling the micropillars. For the FIB process, initially, a Pt layer of ~100nm thick was FIB-deposited homogenously on the selected specimen surface to protect lamellar microstructure from ion damage. The procedure of FIB milling

consisted of a series of concentric annular pattern milling steps using a current from 60nA for the initial coarse milling step, to 50pA for the last fine milling step. Specifically, pillars of diameter ranging from 1 to 7.5μm were milled, with the height-to-diameter ratio kept as 2.5: 1.

Compression of the fabricated micropillars was performed at RT (~20 ^{o}C) by an Agilent G200 Nanoindenter equipped with a flat-end diamond punch in a load-controlled method. Before the compression tests, thermal drift was controlled to below 0.1nm/s and was re-measured to check for consistency during the unloading stage. Loading and unloading were programmed at a constant rate of ~2 MPa/s, with the resultant strain rates of all micropillars within the order of ~10^{-3} /s, and the maximum loads were set at values corresponding to engineering stresses of ~150 MPa for the AC micropillars and ~55 MPa for the FC ones. The morphology of the deformed micropillars was imaged using SEM. Furthermore, TEM (transmission electron microscopy) examination was carried out on longitudinal sections of the deformed micropillars, which were prepared by first FIB milling along the height direction of the micropillar to a thickness of ~1μm, followed by cutting from the bulk substrate and welding onto an Omniprobe by tungsten deposition. The TEM specimens were then finely milled to achieve thicknesses below 150nm after removal from the Omniprobe and welding onto copper TEM grids. TEM examination was carried out in an FEI Tecnai G2 20 Scanning TEM at 200kV.

3. Experimental Results

Fig. 1(a) and (c) show typical microstructures of the eutectic Sn/Pb alloys. Alternate lamellae of β-Sn (dark phase) and Pb (light phase) are homogenously distributed. Using the line-intercept method, the lamellar thicknesses of β-Sn in the air-cooled (AC) and slow furnace-cooled (FC) alloys were measured to be ~1.5 and ~3.5μm, respectively, and those for the Pb phase were ~0.45 and ~1.05μm, respectively. The AC microstructure exhibits finer lamellar structures than the FC,

which agrees with previous findings that the cooling rate significantly determines the lamellar structure of Sn/Pb alloys [47]. Fig. 1(b) and (d) show the nominal strain-stress curves of the AC and FC eutectic Sn/Pb micropillars along the direction ~[001]. In both cases, significant stress avalanche occurred with specimen sizes below 3.5μm, where the applied stress rapidly dropped with prominent strain increments of ~0.15. Larger specimens exhibit smoother deformation with reduced strain. The 2% proof strength $\sigma_{0.02}$ of the eutectic Sn/Pb micropillars measured from the strain-stress graphs are plotted in Fig. 2(a). It can be seen that as the specimen size *D* increases, the 2% proof $\sigma_{0.02}$ strength of both AC and FC eutectic micropillars increases in the size regime from 1 to ~3.5μm, which corresponds to an unusual 'smaller-being-weaker' size effect compared with the conventional "smaller-being-stronger" behavior in monolithic metals [2, 5, 29, 48]. As the specimen size increases beyond ~3.5μm, the strength of both types of Sn/Pb micropillars becomes insensitive to specimen size and tends towards the bulk value. The strength-size trend even in the sensitive regime is not describable by the conventional power law, even with a positive power exponent of size. Fig. 2(a) further indicates that the strength of AC eutectic Sn/Pb with a finer lamellar microstructure is larger than that of the FC state with a coarser lamellar microstructure, with strengths at ~87MPa and ~30MPa at *D* ~7.5μm, respectively. Meanwhile, the 'smaller-being-weaker' size effect of the FC samples with coarser lamellar structure is much milder than the AC case. Fig. 2(b) shows typical morphologies of deformed AC and FC eutectic Sn/Pb micropillars with size of 2.5μm. Interestingly, it can been that alternate lamellae were separated by fracturing along the interphase boundaries (IPBs) after serious straining to more than 0.2 strain. Such fracturing along IPBs should correspond to the last avalanche or load drop in the stress-strain curves shown in Fig. 1(b,d) before the end of the tests. It is also interesting to see from Fig. 1(b,d) that, after the large avalanche corresponding to IPB fracture, the stress rose rapidly,

especially for the smaller specimens with a lower strength. This is due to the diamond punch touching and compressing the top of the lower fractured lamella after the IPB fracture, and when the load reached the maximum value programmed, the specimen was unloaded. In Fig. 2(b), dense and fine slip steps, as commonly appearing in deformed micro metals [49-51], are hardly observed on the micropillar surfaces, in accordance with the smoother stress-strain curves of the 2.5μm specimens in Fig. 1, as compared with the more jerky flow in monolithic metals [49-51]. The majority of the deformed Sn/Pb micropillars actually exhibited similar behavior, and the more gradual stress drops in the smaller specimens in Fig. 1 are therefore likely the result of plasticity or fracture mainly concentrated regions of the IPBs.

Fig.3 (a) and (c) show typical bright-field TEM images in deformed eutectic AC and FC Sn/Pb micropillars with size of 5μm with beam direction (BD) ~ [001]. Short dislocation segments can be seen distributed in the matrix of the Sn phase. The Pb phase was significantly unstable and easily annihilated under the irradiation of FIB during the thinning process, even with voltage reduced to below 10kV. Because of such a technical difficulty, we can only report on the plastic deformation of the Sn lamellae. The dislocation density was measured from TEM images similar to those shown in Figs. 3(a) and (c) by the line-intercepting method, i.e. several lines were randomly drawn on the TEM images to work out the average spacing l of neighboring dislocations, and the dislocation density was calculated as $\rho \sim 1/l^2$. The residual dislocation density of deformed AC and FC Sn/Pb micropillars estimated this way from TEM images taken under the diffraction condition of BD~[001] and g = (220) are plotted in Fig. 3(b) and (d) respectively. (Densities measured under another diffraction vector of g = (200) show similar trends; see Supplementary Materials.) It can be seen that the ρ values of Sn/Pb micropillars deformed to comparable peak stresses could reach as high as ~$10^{15} m^{-2}$, and exhibit an increasing trend as the specimen size

increases. In either groups of AC and FC, although the pillars of different sizes were not compressed to the same final strain, they were compressed to comparable peak stresses, so that the larger specimens in each group had smaller strains (see Fig. 1), and yet their residual dislocation density was still higher than the smaller pillars (see Fig. 3). Also of significance from Figs. 3(b) and (d) is that the residual dislocation density of the AC specimens is almost ~1.5 times of the FC counterparts of the same size, and considering also that strength of the AC micropillars is higher as shown in Fig. 2(a), strength in the present eutectic micropillars is evidently controlled by dislocation interactions rather than by dislocation starvation.

4. Modeling methods

In order to understand the unusual 'smaller-being-stronger' size effect discovered in the present lamellar microstructure of the Sn/Pb system, modeling based on two different methods was carried out, with an objective to incorporate the effects of both the intrinsic microstructural length scale of the lamellar spacing, and the external specimen scale.

4.1. Continuum dislocation model

The accumulation of mobile dislocations during deformation of a lamellar micropillar is estimated quantitatively following a previous model for the precipitated microstructure [31]. The rate of change of the mobile dislocation density $\dot{\rho}_m$ is expressed as

$$\dot{\rho}_m = N_d C \sigma^n - \frac{\rho_m \bar{v}}{k\Lambda}, \quad (1)$$

where the first term accounts for dislocation generation while the second term annihilation. Here, Λ stands for the mean free path of mobile dislocations before they become trapped by dislocation forests, captured on an interphase boundary (IPB), or annihilated on a free surface, $\bar{v}$ is the mean velocity of dislocation glide, σ is the applied stress which, in the present experimental condition,

evolves with time t at a fixed rate $\dot{\sigma}$ so that $\sigma = \dot{\sigma}t$, and C and n are constants. In a lamellar microstructure, it is assumed that dislocation sources are present on the IPBs as well as within the interiors of the lamellae, and a geometric parameter N_d is used to reflect the relative importance of IPBs in generating dislocations in the micro-specimen, as

$$N_d \approx 1 + \frac{2r\, h_{IPB}}{d_1+d_2}\left(1 + \frac{\tan\theta}{R}\right), \tag{2}$$

where h_{IPB} is the thickness of each IPB, d_1 and d_2 are the thicknesses of the two lamellar phases respectively, θ is the inclination from the basal plane of micropillar of the lamellae which are assumed to be parallel, R is the height-to-diameter ratio of the micropillar, and r is the ratio of the density of dislocation sources in the IPBs to that within the lamellae. The value of θ is taken to be ~60° in accordance with experimental observation, and other values in eqn. (2) are given in Table 1.

Meanwhile, the IPBs are also dislocation sinks, as similar to grain boundaries [39, 46, 52]. Hence, according to Carlton and Ferreira's model initially proposed for grain boundaries, the probability P_{dis} of a mobile dislocation absorbed by an IPB on an atom-by-atom basis is assumed to be [39, 53],

$$p_{dis} = \left\{1 - \left[1 - \exp\left(\frac{-(\Delta G + \tau b^3)}{k_B T}\right)\right]^{\frac{sb\nu}{\dot{\varepsilon} d}}\right\}^{\omega L}, \tag{3}$$

where $\Delta G$is the activation energy for an atom to successfully jump into the IPB, $N = sb\nu/\dot{\varepsilon}d$ is the number of jump attempts of atoms in the dislocation core to the IPB within a given time, b is the magnitude of Burgers vector, ν is the Debby frequency, d is the thickness of lamellae, $\dot{\varepsilon}$ is the strain rate calculated at current simulation step, $J = \omega L$ is the total number of atoms on the dislocation core jumping into the IPB, ω is the average linear density of atoms on the dislocation core of length L, k_B is the Boltzmann constant, $T = 293K$ for RT, τ is the resolved shear stress

assumed as $\tau = s \cdot \sigma$ and s is the Schmid factor. The values used for the above parameters are given in Table 1. In particular, the values of ΔG are taken to be the activation energy for migration of eutectic Sn/Pb IPBs at low temperatures which takes place via an atomic jumping process similar to the present assumed process for dislocation absorption [54]. For the Schmid factor, the orientation of Sn lamellae along the micropillar axis is ~ [001], hence the maximum Schmid factor s for the Sn phase is ~0.229 for $(011)[0\bar{1}1]$, among the 9 possible slip systems in the body-centered tetragonal unit cell of Sn with *c*/*a* = 0.5457 [54, 55]. For the Pb phase, the lamellae were too thin to be detected by EBSD, and so their Schmid factor was estimated from the preferred crystallographic relationship of the eutectic Sn/Pb IPBs of $(1\bar{1}\bar{1})_{Pb} \parallel (011)_{Sn}$ and $[211]_{Pb} \parallel [211]_{Sn}$ [54, 56], which well matches the observed inclination θ of lamellae from the basal plane ($\sim 61.38°$ according to the crystallographic relation while ~60° as observed). By this relation the $(\bar{1}1\bar{1})$ [110] slip system of the face-centered-cubic Pb was found to exhibit the maximum Schmid factor of ~0.206. The mean length *L* of dislocations is assumed to be ~100 *b*, as a typical length scale in a micropillar, and values of other parameters in eqn. (3) are listed in Table 1.

Generally, the value of Λ of mobile dislocations is mainly governed by the mutual interactions of dislocations which, in bulk metals with a low density of impurities, would normally lead to prevalent strain hardening, or formation of sub-structures like cells and subgrains. Moreover, in a micro-sized specimen with a lamellar microstructure, the IPBs, the lamellae with their spacing as an intrinsic length scale *d*, and the specimen dimension as an external scale length *D*, would affect the elimination of mobile dislocations by IPB capture and free-surface annihilation. Therefore, the mean path length Λ is given as [39, 57],

$$\frac{1}{\Lambda_1} = \frac{1-P_1^{dis}}{d_1} f(d_1) + \frac{1-f(d_1)}{D} + \gamma\sqrt{\rho_1^{tot}}, \quad (4)$$

$$\frac{1}{\Lambda_2} = \frac{1-P_2^{dis}}{d_2} f(d_2) + \frac{1-f(d_2)}{D} + \gamma\sqrt{\rho_2^{tot}}, \tag{5}$$

where the index 1 and 2 stand for the two lamellar phases respectively, ρ^{tot} is total dislocation density accumulated inside each lamellar phase, γ is a strain-hardening coefficient, $f(d)$ is a function expressing the ability of an IPB to conserve dislocations due to purely geometrical effects as illustrated in Fig. 4(a). Here, a flat lamella of thickness d is assumed to incline at an angle θ inside a pillar of diameter D. This lamella would have a volume πABd, where $A = D/(2\cos\theta)$ is the semi-major axis and $B = D/2$ the semi-minor axis of the elliptical lamella plane. A part of the lamella volume, denoted by the shaded volume $V(d)$ in Fig. 4(a), would be the volume in which all gliding dislocations would encounter the lower IPB shown and be captured by it, whilst other dislocations moving in the rest of the lamella volume would glide and annihilate at the free surface. Hence, the ratio $f(d) = V(d)/(\pi ABd)$ quantitatively indicates the ratio of the mobile dislocations exhausted by IPB trapping, relative to those exhausted by free-surface annihilation. The function $f(d)$ can be calculated as

$$f(d) = \frac{V(d)}{\pi ABd} = \begin{cases} \frac{1}{2} - \frac{1}{3\pi A^2 d}\frac{k_1k_2}{k_2-k_1}\left[A^2 - \left(\frac{d}{k_1} - \frac{d}{k_2} + A\right)^2\right]^{\frac{3}{2}} + \frac{1}{\pi d}\frac{k_1k_2}{k_2-k_1}\sqrt{A^2 - \left(\frac{d}{k_1} - \frac{d}{k_2} + A\right)^2} \\ \quad + \frac{1}{\pi d}\frac{k_1k_2}{k_2-k_1}\left(\frac{d}{k_1} - \frac{d}{k_2} + A\right)\sin^{-1}\frac{\left(\frac{d}{k_1} - \frac{d}{k_2} + A\right)}{a} - \frac{A}{2d}\frac{k_1k_2}{k_2-k_1}, & \text{if } \frac{d}{k_2} - \frac{d}{k_1} \le 2A \\ -\frac{A}{d}\frac{k_1k_2}{k_1-k_2}, & \text{if } \frac{d}{k_2} - \frac{d}{k_1} > 2A \end{cases}, \tag{6}$$

where $k_1 = \tan\varphi$, $k_2 = -\cot\theta$ and φ is the inclination of the glide plane from the basal plane of the micropillar. Generally, $f(d)$ exhibits a prominent dependence on intrinsic and external scale length, as shown in Fig. 4(b), and it always drops rapidly with increasing lamellar spacing, especially for D smaller than ~2.5 μm where plasticity is governed by the conventional mechanism of dislocation exhaustion at free surfaces, with less pile-up takes place adjacent to the IPBs of thicker lamellae. Meanwhile, as D increases $f(d)$ also increases, because dislocations gliding in the lamella interior of a larger specimen would have a higher probability of encountering an IPB,

which may aggravate pile-up against the IPB. The result indicates that the specimen may be strengthened in a similar way as the Hall-Patch relation in bulk materials due to the back stress from the dense dislocations piled up on the IPBs which will hinder the mobility of the forthcoming dislocations.

In Eq. (1), the velocity law is assumed as $\bar{v} = k_v\left(\sigma_{eff}\right)^m$ where k_v and m are constants, and the effective stress σ_{eff} is given by

$$\sigma_{eff} = \dot{\sigma}t - \sigma_f - \alpha\sqrt{\rho^{tot}} - k_d d^{-0.5}. \tag{7}$$

if σ_{eff} calculated this way is positive, and σ_{eff} is set to zero otherwise. The resistance terms in Eq. (7) are the intrinsic lattice friction σ_f, the Taylor hardening $\alpha\sqrt{\rho^{tot}}$, and Hall-Patch-type hardening $k_d d^{-0.5}$ due to the IPBs, respectively. The total dislocation density ρ^{tot} includes all dislocations not escaping out to a free surface nor absorbed by the IPBs, but conserved inside the volume of the micropillar; hence, the value can be estimated as

$$\rho^{tot} \approx \rho_0 + \left(\int_0^t N_d C\dot{\sigma}^n t^n dt\right) f(d)(1 - P_{dis}) = \rho_0 + \left(\frac{N_d \cdot C}{n+1}\dot{\sigma}^n t^{n+1}\right) f(d)(1 - P_{dis}). \tag{8}$$

Therefore, substituting Eq. (2-8) into Eq. (1), and applying a simple difference scheme to solve the nonlinear differential equation, the evolution of mobile dislocation density can be given as

$$\Delta\rho(t) = \left[N_d C\sigma^n - k_v \frac{\rho_m(\sigma_{eff})^m}{k\Lambda}\right]\Delta t, \tag{9}$$

$$\rho_m(t + \Delta t) = \rho_m(t) + \Delta\rho(t). \tag{10}$$

The strain ε involves elastic and plastic components during deformation, i.e., ε_{el} and ε_{pl} respectively. Generally, the elastic strain ε_{el} of each phase can be given by $\varepsilon_{el} = \sigma/E$ where E is the elastic modulus. With the Orowan equation $\varepsilon_{pl} = \rho_m \bar{v} b = \rho_m b k_v\left(\sigma_{eff}\right)^m$, the plastic strain ε_{pl} is estimated through substituting the results calculated from Eqs. (7) to (10) into the Orowan

relation. Assuming the deformation taking place homogeneously, the total strain of a deforming Sn/Pb micropillar would be

$$\varepsilon^{tot} = \varepsilon_{Sn} V_{Sn} + \varepsilon_{Pb} V_{Pb} \tag{11}$$

wherein $V_{Sn} = 0.7266$ and $V_{Pb} = 0.2734$ are volume fractions of Sn and Pb phases in the present eutectic Sn/Pb alloys respectively. The values of parameters used in this theoretical model are listed in Table. 1.

4.2. Two-dimensional discrete dislocation dynamics model

Two-dimensional discrete dislocation dynamics simulation, developed in previous studies on micro-scaled materials [58, 59], is also used to study the size-effect of strength in eutectic micropillars. The simulation region is set as rectangle with the long and short sides, of aspect ratio 3:1, standing for the surfaces parallel and perpendicular to the axial direction of a micropillar. At such an aspect ratio, free-surface annihilation occurs predominantly on the long sides of the micropillar, and so the free boundary condition is imposed along the long sides, meaning that dislocations there would experience image forces and may annihilate there. On the other hand, the periodic boundary condition is applied along the axial direction of the simulation region, so that dislocations escaping from one side will re-enter the simulation region through the other side. For simplification, screw dislocations are considered as randomly distributed inside the simulation region with an initial density ρ_0. Two orthogonal slip systems orientated at 45° and 135° from the base direction are set in the simulation region. Alternate domains of two phases partition the simulation region and they are separated by interphase boundaries (IPBs) orientated at 60° from the base direction of the simulation region. The IPBs are set as impenetrable by dislocations with an effective thickness of ~150b. Dislocation sources replicating the Frank-Read (FR) type in 3D are randomly distributed in the simulation region with an initial density ρ_{FRS}. These sources

operate as follows: a new dipole of spacing L_{nuc} will be planted at the source position when the local stress exceeds a pre-set critical value τ_{nuc} for a continuous time over 50ms. The dipole spacing is set to be $L_{nuc} = \mu b/2\pi\tau_{nuc}$ so that the dipole will not annihilate under its own attraction, and the critical nucleation stress τ_{nuc} follows a Gaussian distribution whit a mean value of 12 MPa and standard derivation 6 MPa. Each source can be operated once after a relaxation time of 250ms. The initial density ρ_0 and ρ_{FRS} are both set as 2.2 μm^{-2}.

External compressive stress is uniformly applied onto the simulation region along its long axis with a constant loading rate of 2 MPs/s. The pair-wise elastic interaction force f_{ij} of neighboring dislocations *i* and *j* within a cutoff distance of 200*b* is assumed to be $f_{ij} = \mu b^2/2\pi r_{ij}$, where shear modulus μ is set to be 18 GPa and 5.6 GPa respectively for the Sn and Pb phase regions [55]; b is the magnitude of the Burgers vector, as ~0.66nm and ~0.35nm for Sn and Pb phase respectively[29, 55, 60]; and r_{ij} is the distance between dislocations *i* and *j*. Mobile dislocations gliding near a free surface within a cutoff distance will experience an image force according to the relation of f_{ij} above, with an image dislocation of opposite sign placed appropriately outside the simulation region. Moreover, Taylor hardening is simulated by introducing a resistance stress as $\tau_{forest} = \alpha\sqrt{\rho_{tot}}$, where ρ_{tot} is the residual dislocation in each phase domain and α=0.285 is constant. Hence the resultant glide stress τ_i of each dislocation *i* resolved on its slip system can be calculated, and then velocity is calculated as $v_i = k\tau_i$ where *k* is assumed to be 0.72 μm/MPa·s. The exact value of *k* in the two eutectic phases is not known, but this parameter is usually set to be within the range 0.5 to 1.5 μm/MPa·s in DD simulations [58, 59, 61], and changing it within such a range was found to produce no significant differences in the results. Once a mobile dislocation encounters an IPB, it will be considered as pinned up by the latter. Also, as aforementioned, IPBs

also acts as dislocation sinks, and hence the pinned-up dislocation is set to have a probability to annihilate, which is taken to be the p_{dis} in eqn. (3). The strain increment in each time step is calculated through the Orowan relation as $\Delta\varepsilon = \sum_{i=1}^{N_m} v_i b \cdot \Delta t/\Omega$ where Ω is the area of simulation region and N_m is the number of mobile dislocations during the current time step. The size of simulation width is selected from 1.5 to 7.5μm correspond to the micropillars in the actual experiments. For direct comparison with the experiments, the lamellar spacing (SP) is set to be 1.0, 1.5 or 2.0μm which are in the range of the experimental values for both the AC and FC conditions of the Sn/Pb alloy.

5. Discussion

5.1. Continuum dislocation model

The predicted density of mobile dislocations and the total density of all dislocations in Sn/Pb micropillars with different lamellar spacings corresponding to the AC and FC experimental conditions are plotted in Fig. 5(a) and (b), respectively. As the specimen size increases, the accumulation of dislocations increases, which well matches the TEM observations, as shown in Fig. 3(b) and (d). The loss of dislocations is significantly reduced in a larger specimen because, on the one hand, dislocations can hardly zip through the thickness of a large pillar, but remain inside to form obstacles for the subsequent dislocations, and on the other hand, a larger micropillar contains more IPBs, which not only provide sites for dislocation nucleation but also trap dislocations. Therefore, the accumulation of dislocations is prominently enhanced in larger specimens. Although more dislocations are retained with straining, the net quantity of mobile dislocations initially rises up to a critical applied-stress point, and then drops afterwards as shown in mechanical properties of Sn and Pb are used in the two phases (a), and the critical applied stress when the density of mobile dislocations begins to reduce occurs earlier as the micropillar size decreases.

To understand this, we notice that that free path Λ of dislocations in specimens smaller than ~ 3 μm is quite close to the pillar size itself as Fig. 5(c) and (d) show. This indicates that in these smaller pillars, mobile dislocations are quickly exhausted through surface annihilation due to the low value of $f(d)$ as shown in Fig. 4(b). The low efficiency for the IPBs to trap dislocations explains why the critical point in the evolution curve of the mobile-dislocation density appears earlier in smaller specimens. Comparing the simulations for the AC and FC conditions, micropillars with a finer lamellar microstructure (AC) can maintain more dislocations anytime, owing to the larger amounts of IPBs present which serve to retain the dislocations. Therefore a finer lamellar microstructure can significantly strengthen the micro specimen.

In order to investigate the size-dependent relation between the mean free path Λ and the characteristic length scales in eutectic micro-specimens, the Λ free of strain, i.e. $\varepsilon = 0$, versus the lamellar thickness *d* and micropillar size *D* is plotted in Fig. 4(c), with the initial dislocation density $\rho_0^{tot} = 2.2\ \mu m^{-2}$. The result shows that Λ initially increases with increasing *D* in the regime where *D* is smaller than the lamellar spacing, and for specimen sizes larger than the lamellar spacing, Λ starts to adopt the value of the lamellar spacing *d*. Since the Sb phase has a significantly larger volume fraction in the eutectic Sn/Pb micropillars, the plastic deformation in the Sb lamellae dominates the deformation of the entire micropillar. Fig. 5(c) and (d) show that in the Sn lamellae, Λ converges to a range close to the lamellar spacing *d* for specimens larger than ~2μm, due to the fact that more dislocations are retained inside the lamellar volume bounded by two adjacent IPBs. Hence the steady value of mean path Λ simply becomes the lamellar thickness *d* which constrains the gliding space of mobile dislocations as expected. Meanwhile, Λ appears to decrease gradually with increasing strain (or stress) due to the propagation of dislocations which enhances their mutual interactions. Besides, the Λ of the 1 μm-specimen is significantly small at ~ 1 μm, in good

agreement with the dislocation density plotted in Fig. 5(a) which indicates significant dislocation exhaustion by surface annihilation.

Then, inputting the evolution of the predicted dislocation density and mean free path into Eq. (11), the 2% proof strength $\sigma_{0.02}$ was calculated as shown in Fig. 4(d). The predicted $\sigma_{0.02}$ matches well with the experimental results, namely a 'smaller-being-weaker' size-dependent trend occurs. Interestingly, $\sigma_{0.02}$ turns steady as a constant value of ~90 MPa for specimens larger than 3.5μm, whilst it drops to ~65 MPa as specimen size decreases to 1.0 μm, in the case of the AC condition with lamellar spacing of 1.5 and 0.45μm for the Sn and Pb phases respectively. The drop in strength is more prominent in the AC condition with a finer lamellar microstructure compared to the FC condition. Furthermore, the calculated density of mobile dislocations at ~2% strain versus specimen size *D* exhibits a similar trend as the $\sigma_{0.02}$. Hence, according to the Orowan relation $\varepsilon_{pl} = \rho_m \bar{v} b$, the 'smaller-being-weaker' size effect is mainly due to two factors: on one hand, mobile dislocations in micropillars smaller than 3.5μm can easily zip through the specimen thickness since the few IPBs present can hardly trap them, according to the $f(d)$ trend in Fig. 4(b); on the other hand, sources for dislocation nucleation are also reduced with fewer IPBs. The accumulation of dislocations inside a small volume is impaired and hence potential dislocation pileup and forest interactions are highly reduced, leading to a low resistance on the subsequent dislocations gliding in the crystal. Therefore, the increase of the effective stress σ_{eff} offsets the loss of mobile dislocations in the Orowan relation to maintain a stable strain rate, without the need to activate more mobile dislocations by applying a higher external stress. On the contrary, in specimens larger than ~3.5 μm, the more IPBs present are efficient in blocking dislocations inside the specimen, which highly enhances strength. The result is the softening trend in specimens smaller than 3.5μm. Due to the fact that a finer lamellar microstructure is more effective in improving the accumulation

of dislocations, it is also understandable that the 'smaller-being-weaker' effect is more prominent in the AC specimens.

5.2. Discrete dislocation dynamics modeling

It should first be mentioned that the discrete dislocation dynamics simulations carried out were 2D while dislocation activities in reality are 3D; therefore the simulations here only provide qualitative predictions of trends while the length scales involved, such as the lamellar spacing (SP), may not be directly comparable to the 3D reality.

Fig. 6(a) shows the relation between 2% poof strength and simulated specimen size *D* for different lamellar spacing (SP) values of 1, 1.5 and 2 μm. This range of SP values roughly covers the conditions in the AC and FC alloys in the experiments – in the AC alloy, the lamellar thicknesses of the two phases were 1.5 μm and 0.45 μm, thus an average of ~ 1 μm, and in the FC alloy, the phase thicknesses were 3.5 μm and 1.05 μm, with an average close to 2 μm. As the SP varies from 1 to 2 μm, the trend of 2% proof strength versus *D* exhibits distinctively different scenarios. In the case of SP = 1 μm, the "smaller-being-weaker" trend is predicted, as the 2% proof strength decreases with decreasing specimen size in the regime below ~3.5μm. However, as SP increases to 1.5μm, the 2% proof strength becomes insensitive to the specimen size, and as SP = 2μm, the "smaller-being-stronger" phenomenon is predicted, in which strength increases with decreasing specimen size in the regime below ~3.5μm. The "smaller-being-weaker" trend at SP = 1 μm is similar to the case found for the AC Sn/Pb samples in Fig. 2(a), in which the phase thicknesses were also similar at 1.5 μm and 0.45 μm. On the other hand, the FC samples had larger phase thicknesses of 3.5 μm and 1.05 μm and their size effect is flat in Fig. 2(a), and the simulated size effect in Fig. 6(a) at SP = 1.5 μm is indeed flat, although that at SP = 2 μm has transited to "smaller-being-stronger". The 2D simulations here may not capture exactly the quantitative

aspects of the experiments, but they indicate that, as the lamellar spacing is increased, the size effect of strength in lamellar micropillars should transform from a "smaller-being-weaker" trend to one insensitive to size, which is what the present AC and FC samples show. Although the further "smaller-being-stronger" effect is not seen from the present experiments in Fig. 2(a), it is expected that as the lamellar microstructure is further coarsened, this behavior should arise.

Fig. 6(b) and (c) show the simulated density of mobile dislocations and the total dislocation density at ~2% strain at different lamellar spacing. At all three values of lamellar spacing simulated, both the mobile and total densities increase on increasing specimen size up to ~3.5μm, beyond which the density of both types of dislocations saturates to constant values. The low dislocation density in the size regime smaller than ~3.5μm indicates significant dislocation exhaustion by free-surface annihilation due to ineffective blockage by the IPBs. Meanwhile, the residual density of mobile dislocations is predicted to increase by approximately $1 \times 10^{12} \mathrm{m}^{-2}$ for every reduction by ~0.5 μm in the lamellar spacing at any specimen size. This is obvious as a smaller lamellar spacing would mean more IPBs present, which would lead to more dislocations retained inside the specimen. Thus, in the case of the smallest lamellar spacing of 1 μm, the quantity of dislocations retained by the IPBs is high, even for the smallest specimen size simulated, and in this density range, strength is dominated by dislocation interactions, rather than by dislocation starvation as in monolithic specimens with very low dislocation contents. Thus, the "smaller-being-weaker" trend in this case follows closely the trend of dislocation density vs specimen size, namely, as the specimen size decreases to below 3.5μm, strength diminishes due to fewer dislocations retained inside the specimen by the IPBs, thus reducing the mutual interactions between dislocations. On the other hand, for the largest lamellar spacing of 2 μm simulated, lack of trapping by IPBs leads to an overall starvation or exhaustion state of the dislocations, and at such a low dislocation content,

mutual interactions become insignificant, and strength is dominated by the starvation mechanism. To sustain the deformation, high applied stresses are needed to replenish the escaped dislocations by new nucleation, and this explains the "smaller-being-stronger" size effect. At the intermediate lamellar spacing of ~1.5 μm, dislocation retention by the IPBs is intermediate, and the two factors governing strength as discussed above, namely, mutual interactions vs starvation, more or less balance out, and the result is a rather insensitive size effect of strength, as shown in Fig. 6(a).

The findings here lead to the interesting conclusion that the size effect of strength in micro-specimens is actually tunable by engineering the internal length scale of the microstructure. The present experiments on the eutectic, lamellar microstructure illustrate this well, and future work should explore this effect in other types of microstructures. We also note in passing that, in the light of the present observed "smaller-being-weaker" phenomenon, the strength of eutectic solders may be significantly weakened when they are applied to micro-scaled mechanical/electrical systems approaching to the micron dimensions. Such a weakening effect may have important implications in the reliability of micro-scaled devices.

6. Conclusions

To conclude, an unusual 'smaller-being-weaker' size effect on strength is found in micro-scaled eutectic Sn/Pb alloys. This size effect occurs when strength is governed by mutual dislocation interactions, rather than by dislocation starvation, and so is expected to happen in a finer lamellar microstructure which retains higher contents of residual dislocations. Prominent strengthening arises in large specimens through Taylor hardening and mutual dislocation interactions as a result of significant dislocation retention by the interphase boundaries, but this dies down in small specimens in which fewer interphase boundaries are present to block mobile dislocations from gliding to and eliminating at free surfaces. In a coarser lamellar microstructure, too few interphase

boundaries may be present to produce any significant dislocation retaining effect, and significant loss of gliding dislocations at free surfaces may lead to a dislocation starved state in which the size effect of strength may become a lot milder, or even exhibit the conventional "smaller-being-stronger" behavior.

Acknowledgement

The work described in this paper is supported by funding from the Kingboard Professorship Endowment.

References

[1] M.D. Uchic, D.M. Dimiduk, J.N. Florando, W.D. Nix, Sample dimensions influence strength and crystal plasticity, Science 305 (2004) 986-9.

[2] D.M. Dimiduk, M.D. Uchic, T.A. Parthasarathy, Size-affected single-slip behavior of pure nickel microcrystals, Acta Mater. 53 (2005) 4065-4077.

[3] J. Greer, W. Nix, Nanoscale gold pillars strengthened through dislocation starvation, Physical Review B 73 (2006).

[4] S.S. Brenner, Tensile strength of whiskers, J. Appl. Phys 27 (1956) 1484.

[5] H. Bei, S. Shim, E. George, M. Miller, E. Herbert, G. Pharr, Compressive strengths of molybdenum alloy micro-pillars prepared using a new technique, Scripta Mater. 57 (2007) 397-400.

[6] M.R. Maughan, D.F. Bahr, Discontinuous Yield Behaviors Under Various Pre-Strain Conditions in Metals with Different Crystal Structures, Materials Research Letters 4 (2015) 83-89.

[7] J.R. Greer, C.R. Weinberger, W. Cai, Comparing the strength of f.c.c. and b.c.c. sub-micrometer pillars: Compression experiments and dislocation dynamics simulations, Mat. Sci. Eng. A 493 (2008) 21-25.

[8] R. Dou, B. Derby, A universal scaling law for the strength of metal micropillars and nanowires, Scripta Mater. 61 (2009) 524-527.

[9] K.S. Ng, A.H.W. Ngan, Stochastic nature of plasticity of aluminum micro-pillars, Acta Mater. 56 (2008) 1712-1720.

[10] M. Zaiser, J. Schwerdtfeger, A.S. Schneider, C.P. Frick, B.G. Clark, P.A. Gruber, E. Arzt, Strain bursts in plastically deforming molybdenum micro- and nanopillars, Phil. Mag. 88 (2008) 3861-3874.

[11] M. Dietiker, S. Buzzi, G. Pigozzi, J.F. Löffler, R. Spolenak, Deformation behavior of gold nano-pillars prepared by nanoimprinting and focused ion-beam milling, Acta Mater. 59 (2011) 2180-2192.

[12] H. Tanga, K.W. Schwarzb, H.D. Espinosaa, Dislocation escape-related size effects in single-crystal micropillars under uniaxial compression, Acta Mater. 55 (2007) 1607–1616.

[13] K.S. Ng, A.H.W. Ngan, Stochastic theory for jerky deformation in small crystal volumes with pre-existing dislocations, Phil. Mag. 88 (2008) 677-688.

[14] D. Kiener, A.M. Minor, Source truncation and exhaustion: insights from quantitative in situ TEM tensile testing, Nano letters 11 (2011) 3816-20.
[15] C. Zhou, S.B. Biner, R. LeSar, Discrete dislocation dynamics simulations of plasticity at small scales, Acta Mater. 58 (2010) 1565-1577.
[16] S. Sandfeld, T. Hochrainer, M. Zaiser, P. Gumbsch, Continuum modeling of dislocation plasticity: Theory, numerical implementation, and validation by discrete dislocation simulations, J. Mater. Res. 26 (2011) 623-632.
[17] J.A. El-Awady, S. Bulent Biner, N.M. Ghoniem, A self-consistent boundary element, parametric dislocation dynamics formulation of plastic flow in finite volumes, J. Mech. Phys. Solids. 56 (2008) 2019-2035.
[18] J. Senger, D. Weygand, P. Gumbsch, O. Kraft, Discrete dislocation simulations of the plasticity of micro-pillars under uniaxial loading, Scripta Mater. 58 (2008) 587-590.
[19] S. Akarapu, H.M. Zbib, D.F. Bahr, Analysis of heterogeneous deformation and dislocation dynamics in single crystal micropillars under compression, Int. J. Plasticity 26 (2010) 239-257.
[20] H. Bei, S. Shim, G.M. Pharr, E.P. George, Effects of pre-strain on the compressive stress–strain response of Mo-alloy single-crystal micropillars, Acta Mater. 56 (2008) 4762-4770.
[21] R. Gu, A.H.W. Ngan, Effects of pre-straining and coating on plastic deformation of aluminum micropillars, Acta Mater. 60 (2012) 6102-6111.
[22] C. Zhou, S. Biner, R. LeSar, Simulations of the effect of surface coatings on plasticity at small scales, Scripta Mater. 63 (2010) 1096-1099.
[23] R. Maaß, S. Van Petegem, D. Grolimund, H. Van Swygenhoven, M.D. Uchic, A strong micropillar containing a low angle grain boundary, Applied Physics Letters 91 (2007) 131909.
[24] X.X. Chen, A.H.W. Ngan, Tensile deformation of silver micro-wires of small thickness-to-grain-size ratios, Mat. Sci. Eng. A 539 (2012) 74-84.
[25] D. Jang, J.R. Greer, Size-induced weakening and grain boundary-assisted deformation in 60 nm grained Ni nanopillars, Scripta Mater. 64 (2011) 77-80.
[26] N.L. Okamoto, D. Kashioka, T. Hirato, H. Inui, Specimen- and grain-size dependence of compression deformation behavior in nanocrystalline copper, Int. J. Plasticity 54 (2014) 11.
[27] Y. Kim, S. Lee, J.B. Jeon, Y.J. Kim, B.J. Lee, S.H. Oh, S.M. Han, Effect of a high angle grain boundary on deformation behavior of Al nanopillars, Scripta Mater. 107 (2015) 5.

[28] X. Guo, Q. Guo, Z. Li, G. Fan, D.-B. Xiong, Y. Su, J. Zhang, C.L. Gan, D. Zhang, Interfacial strength and deformation mechanism of SiC–Al composite micro-pillars, Scripta Mater. 114 (2016) 56-59.
[29] C.S. Kaira, S.S. Singh, A. Kirubanandham, N. Chawla, Microscale deformation behavior of bicrystal boundaries in pure tin (Sn) using micropillar compression, Acta Mater. 120 (2016) 56-67.
[30] A. Ngan, X. Chen, P. Leung, R. Gu, K. Gan, Size effects of micrometer-scaled metals—the search continues for materials containing real microstructures, MRS Communications (2017) 1-10.
[31] K. Gan, R. Gu, A.H.W. Ngan, The weakest size of precipitated alloys in the micro-regime: The case of duralumin, J. Mater. Res. 32 (2017) 1-11.
[32] M.M. Ahmed, T.G. Langdon, Ductility of the superplastic Pb-Sn eutectic at room temperature, Journal of Materials Science Letters 2 (1983) 59-62.
[33] C. Kanchanomai, Y. Miyashita, Y. Mutoh, Strain-rate effects on low cycle fatigue mechanism of eutectic Sn–Pb solder, International Journal of Fatigue 24 (2002) 987-993.
[34] D. Grivas, K. Murty, J. Morris, Deformation of Pb-Sn eutectic alloys at relatively high strain rates, Acta Metall 27 (1979) 731-737.
[35] A. Geckinli, C. Barrett, Superplastic deformation of the Pb-Sn eutectic, Journal of Materials Science 11(1976) 510-521.
[36] L. Hachani, K. Zaidat, B. Saadi, X.D. Wang, Y. Fautrelle, Solidification of Sn–Pb alloys: Experiments on the influence of the initial concentration, International Journal of Thermal Sciences 91 (2015) 34-48.
[37] J. Verhoeven, E. Gibson, D. Mourer, The morphology and crystallography of directionally solidified pb-sn eutectic alloys, Metallurgical and Materials Transactions A 8 (1977) 1239-1247.
[38] M.J. Demkowicz, R.G. Hoagland, J.P. Hirth, Interface structure and radiation damage resistance in Cu-Nb multilayer nanocomposites, Phys Rev Lett 100 (2008) 136102.
[39] S. Lei, J.Y. Zhang, J.J. Niu, G. Liu, X. Zhang, J. Sun, Intrinsic size-controlled strain hardening behavior of nanolayered Cu/Zr micropillars, Scripta Mater. 66 (2012) 706-709.
[40] A. Misra, J. Hirth, R. Hoagland, Length-scale-dependent deformation mechanisms in incoherent metallic multilayered composites, Acta Mater. 53 (2005) 4817-4824.

[41] D.M. Dimiduk, P.M. Hazzledine, T.A. Parthasarathy, M.G. Mendiratta, S. Seshagiri, The role of grain size and selected microstructural parameters in strengthening fully lamellar TiAl alloys, Metallurgical and Materials Transactions A 29 (1998) 37-47.
[42] A. Benzerga, S. Hong, K. Kim, A. Needleman, E. Van der Giessen, Smaller is softer: an inverse size effect in a cast aluminum alloy, Acta Mater. 49 (2001) 3071-3083.
[43] T.E.J. Edwards, F. Di Gioacchino, R. Muñoz-Moreno, W.J. Clegg, Deformation of lamellar TiAl alloys by longitudinal twinning, Scripta Mater. 118 (2016) 46-50.
[44] A.J. Palomares-García, I. Sabirov, M.T. Pérez-Prado, J.M. Molina-Aldareguia, Effect of nanoscale thick lamellae on the micromechanical response of a TiAl alloy, Scripta Mater. 139 (2017) 17-21.
[45] C.R. Mayer, L.W. Yang, S.S. Singh, J. Llorca, J.M. Molina-Aldareguia, Y.L. Shen, N. Chawla, Anisotropy, size, and aspect ratio effects on micropillar compression of Al SiC nanolaminate composites, Acta Mater. 114 (2016) 25-32.
[46] R. Fritz, V. Maier-Kiener, D. Lutz, D. Kiener, Interplay between sample size and grain size: Single crystalline vs. ultrafine-grained chromium micropillars, Mat. Sci. Eng. A 674 (2016) 626-633.
[47] Z. Mei, J. Morris, M. Shine, T. Summers, Effects of cooling rate on mechanical properties of near-eutectic tin-lead solder joints, Journal of Electronic Materials 20 (1991) 599-608.
[48] M.A. Meyers, A. Mishra, D.J. Benson, Mechanical properties of nanocrystalline materials, Progress Mater. Sci. 51 (2006) 427-556.
[49] R. Gu, A.H.W. Ngan, Size effect on the deformation behavior of duralumin micropillars, Scripta Mater. 68 (2013) 861-864.
[50] S.W. Lee, W.D. Nix, Size dependence of the yield strength of fcc and bcc metallic micropillars with diameters of a few micrometers, Phil. Mag. 92 (2012) 1238-1260.
[51] C. Zhou, I.J. Beyerlein, R. LeSar, Plastic deformation mechanisms of fcc single crystals at small scales, Acta Mater. 59 (2011) 7673-7682.
[52] R. Kumar, L. Nicola, E. Van der Giessen, Density of grain boundaries and plasticity size effects: A discrete dislocation dynamics study, Mat. Sci. Eng. A 527 (2009) 7-15.
[53] C.E. Carlton, P.J. Ferreira, What is behind the inverse Hall–Petch effect in nanocrystalline materials?, Acta Mater. 55 (2007) 3749-3756.

[54] D. Gupta, K. Vieregge, W. Gust, Interface diffusion in eutectic Pb–Sn solder, Acta Mater. 47 (1998) 5-12.
[55] F. Yang, J. Li, Deformation behavior of tin and some tin alloys, Journal of Materials Science: Materials in Electronics 18 (2007) 191-210.
[56] N. Takahashi, K. Ashinuma, Direct Study of Eutectic Alloys by Means of Electron Microscopy, Journal of the Institute of Metals 87 (1958) 19-23.
[57] U.F. Kocks, A statistical theory of flow stress and work-hardening, Phil. Mag. 13 (1966) 541-566.
[58] P.S.S. Leung, A.H.W. Ngan, Size effect on the strength of micron-sized polycrystals – A dislocation dynamics simulation study, Scripta Mater. 69 (2013) 235-238.
[59] R. Gu, P.P.S. Leung, A.H.W. Ngan, Size effect on deformation of duralumin micropillars – A dislocation dynamics study, Scripta Mater. 76 (2014) 73-76.
[60] W. Hofmann, Lead and lead alloys, Springer, Berlin, Heidelberg, 1970.
[61] K.W. Siu, A.H.W. Ngan, Understanding acoustoplasticity through dislocation dynamics simulations, Phil. Mag. 91 (2011) 4367-4387.

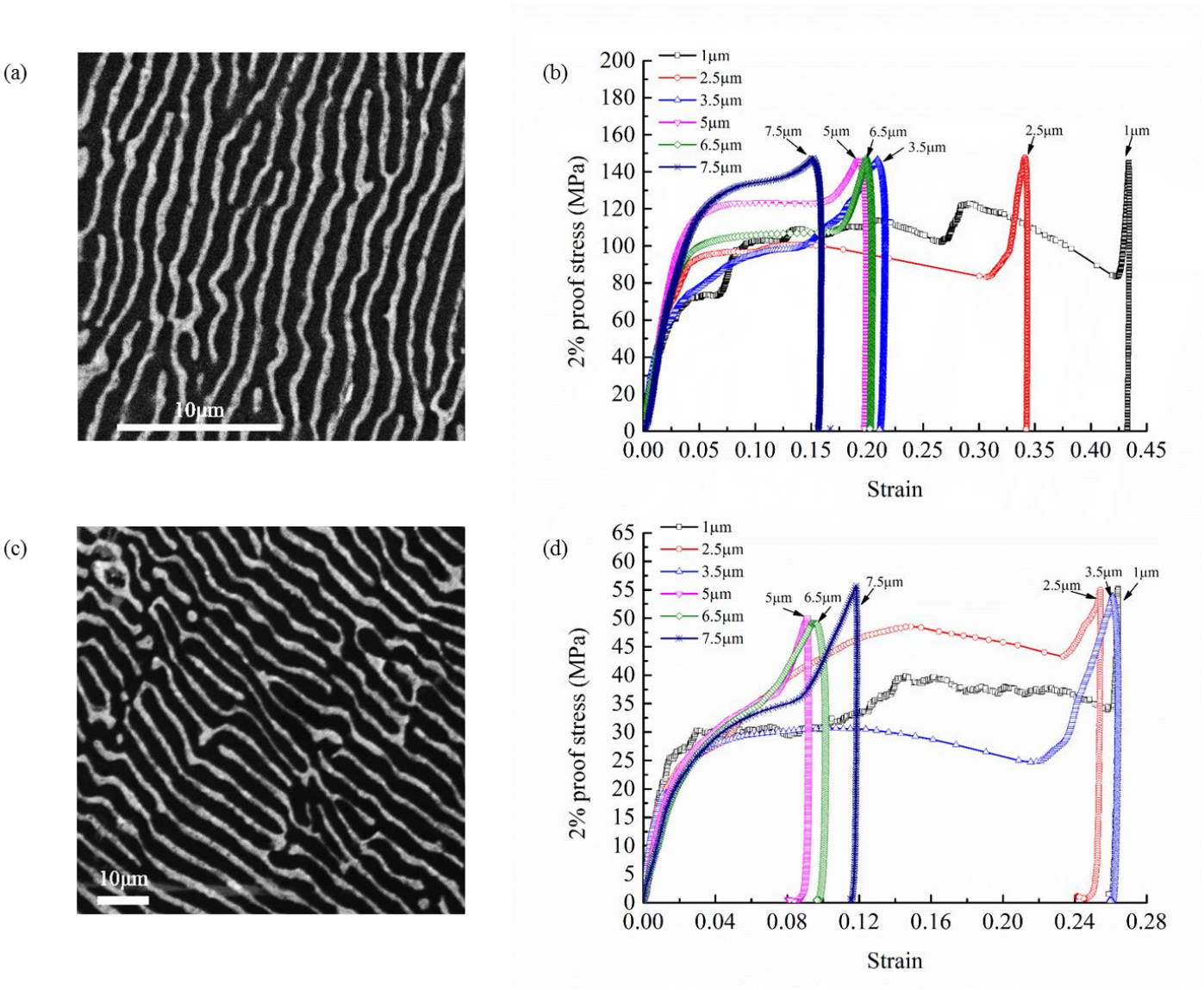

Figure 1. Typical microstructures of eutectic Sn/Pb alloys fabricated through (a) air cooling and (c) furnace cooling respectively (note the difference in the scale bars in the two cases). The dark phase is β-Sn and the white is Pb phase. Nominal strain-stress curves of (b) air-cooled (AC) and (d) furnace-cooled (FC) eutectic Sn/Pb micropillars with different specimen sizes, respectively.

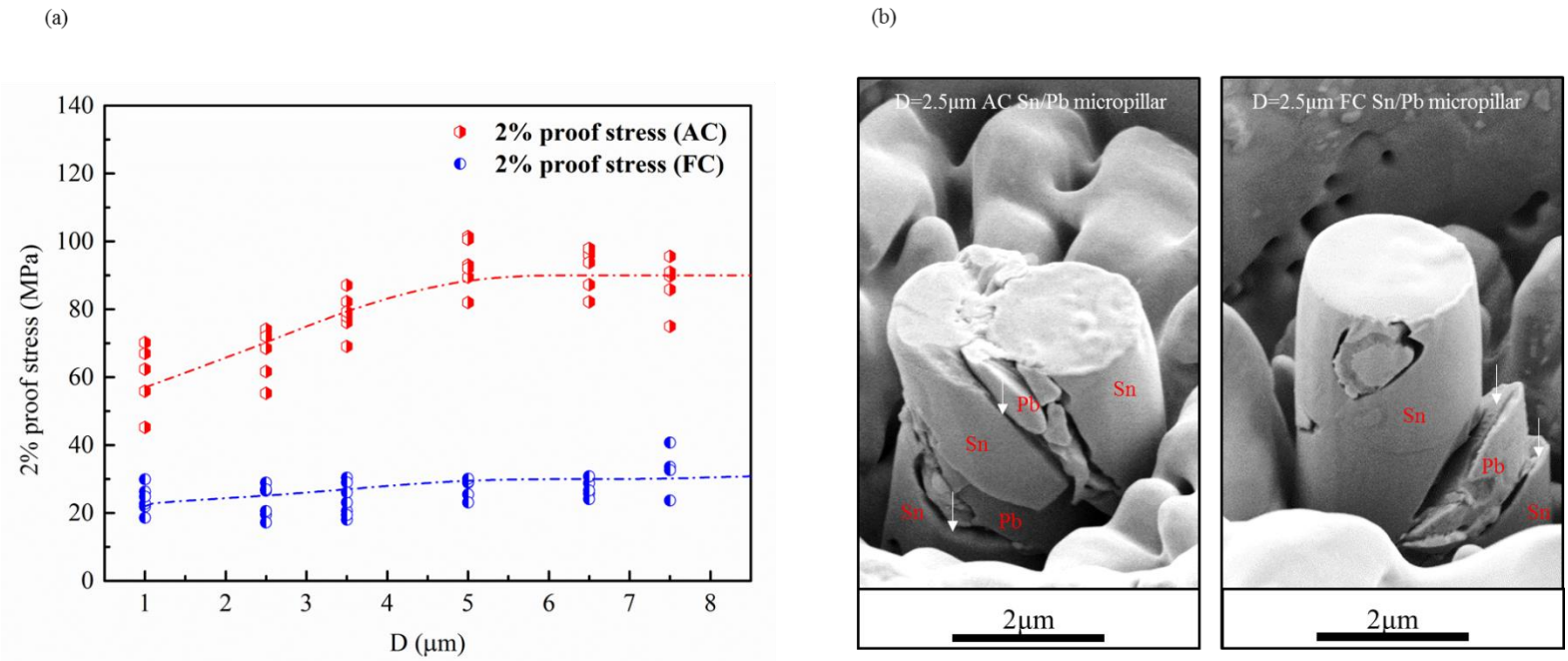

Figure 2. (a) 2% proof strength $\sigma_{0.02}$ vs specimen size *D* in AC and FC treated eutectic Sn/Pb micropillars. (b) Typical SEM morphologies of AC and FC deformed Sn/Pb micropillars with *D* ~2.5μm. Separated interphase boundaries (IPBs) between Sn and Pb lamellas are marked by using white arrows in the images.

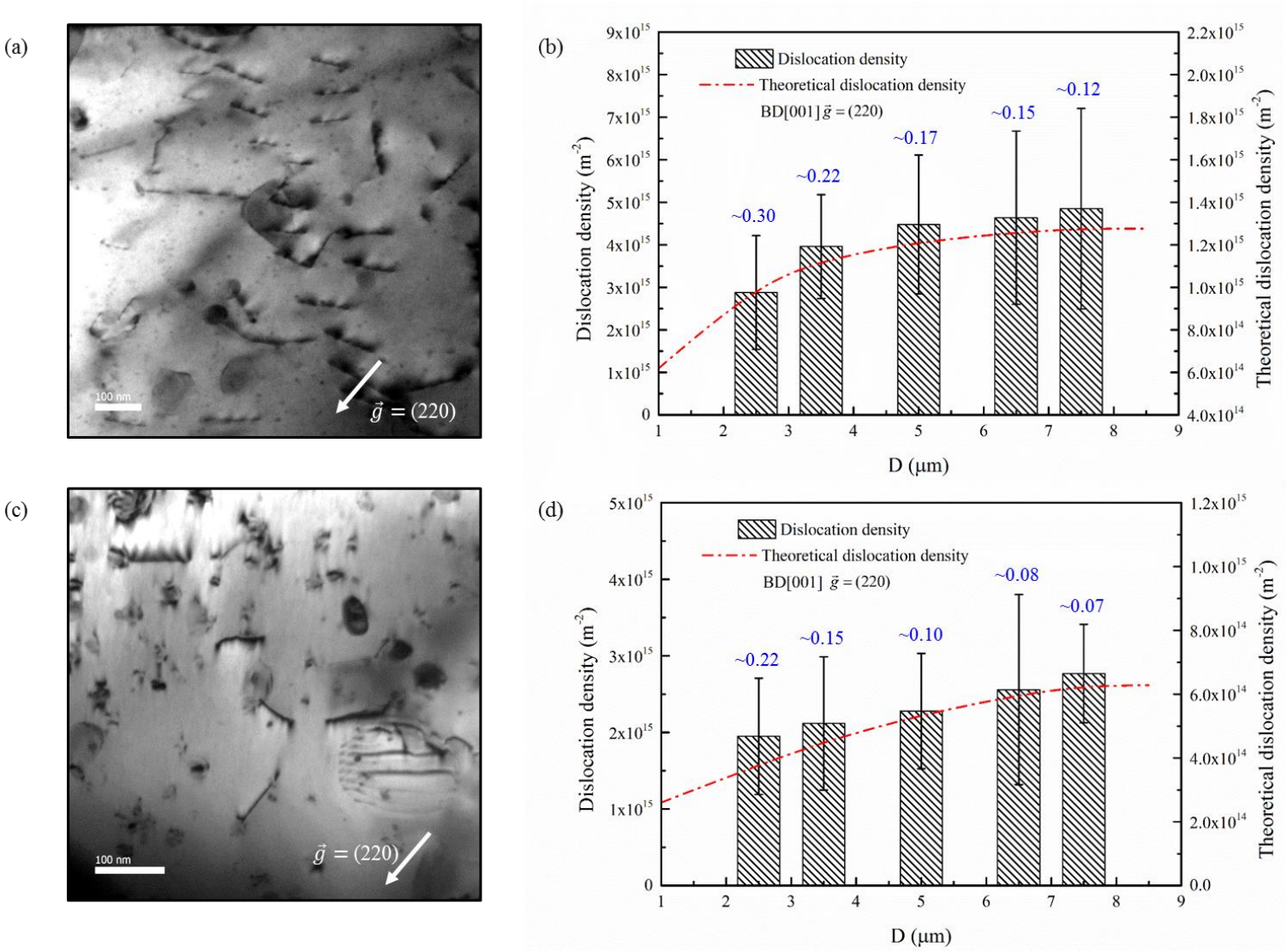

Figure 3. Typical bright-field TEM images of deformed (a) AC and (c) FC eutectic Sn/Pb micropillars with size of 5μm near BD~ [001], respectively. (b) and (d) show residual dislocation density measured through line-interception method in TEM images similar to (a) and (c), for AC and FC samples respectively. Red curves show theoretical prediction discussed in text. The final plastic strains of the micropillars are given in (b) and (d). Despite the larger pillars have lower final strains, their residual dislocation density is still higher than the smaller pillars.

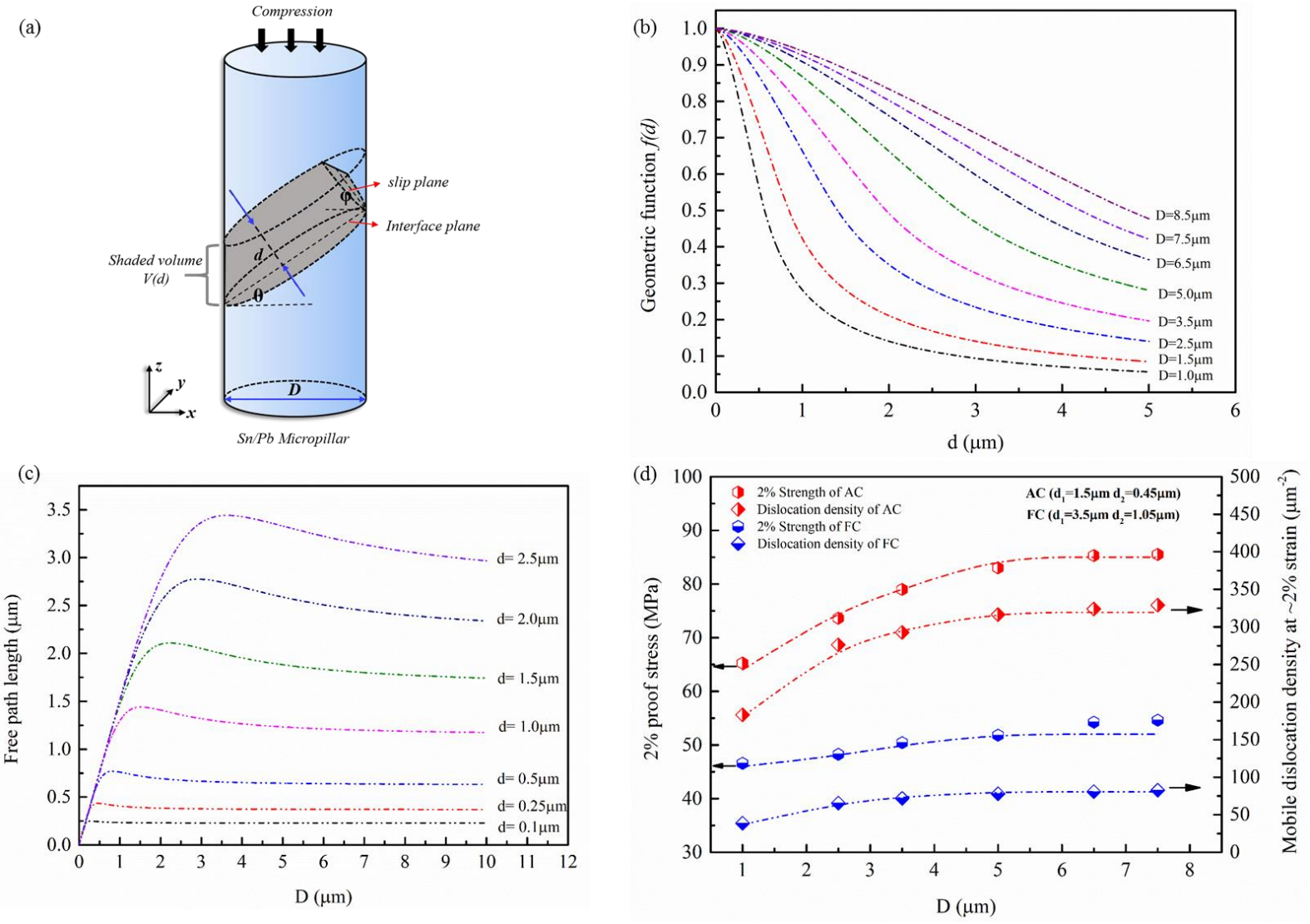

Figure 4. Continuum dislocation model. (a) Schematic of a flat lamella inclined inside a micropillar. (b) Predicted geometric function $f(d)$ versus lamella spacing d for micropillars with different sizes, for the case of $\varphi = 28.6°$ and $\theta = 60°$. (c) The predicted mean free path length Λ versus specimen size D with different lamellar spacing d and initial dislocation density 2.2 μm^{-2} at the beginning of deformation. (d) Estimated 2% proof strength and mobile-dislocation density at ~2% strain in AC and FC eutectic Sn/Pb micropillars with different lamella spacing d, predicted by the continuum dislocation model discussed in text.

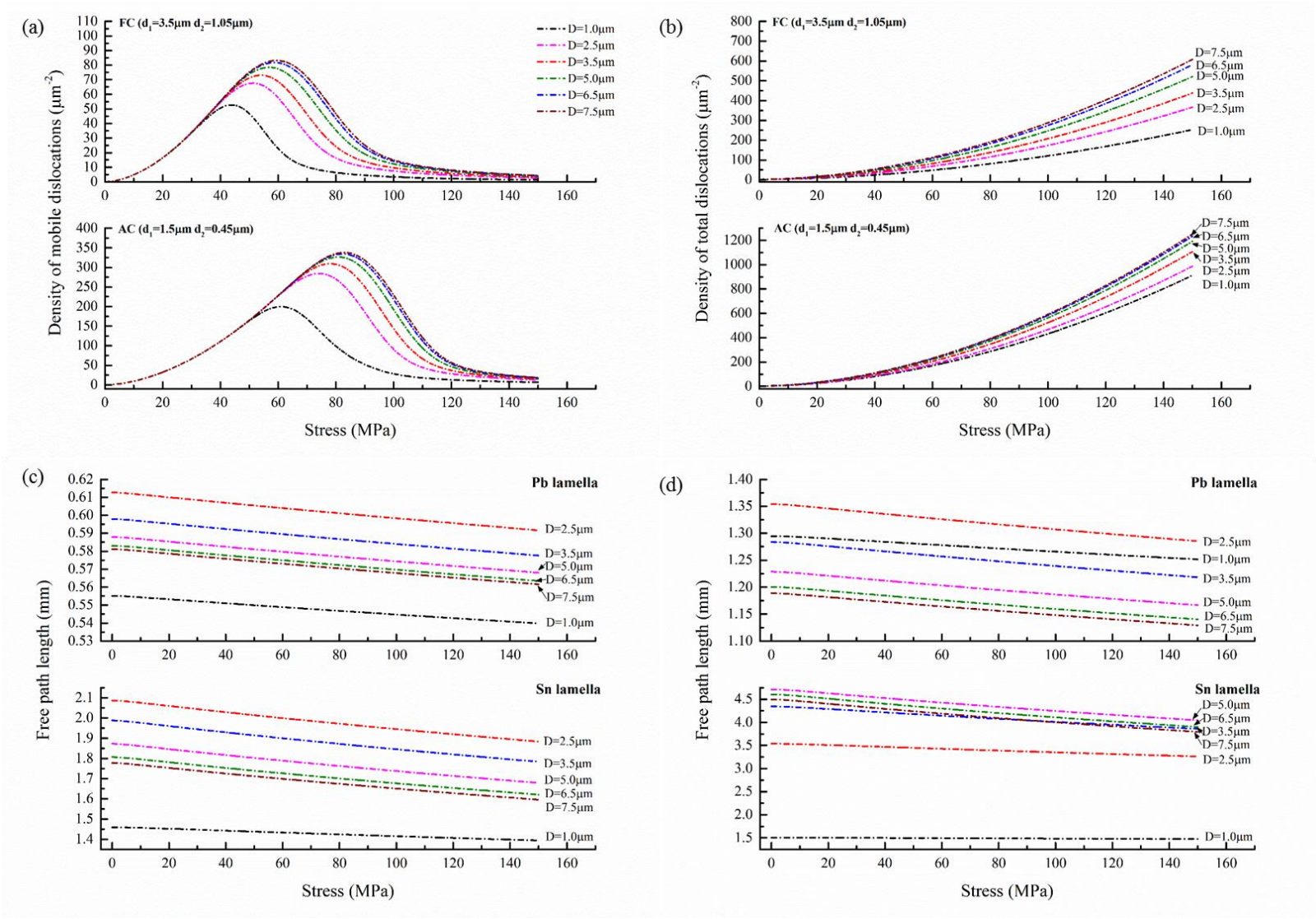

Figure 5. Predictions of continuum dislocation model. (a) and (b) illustrate the predicted evolution of total- and mobile-dislocation density respectively for AC and FC eutectic Sn/Pb micropillars. Predicted evolution of mean free path Λ with applied stress in lamellar Sn and Pb phases of (c) AC and (d) FC Sn/Pb micropillars with specimen size *D*, respectively.

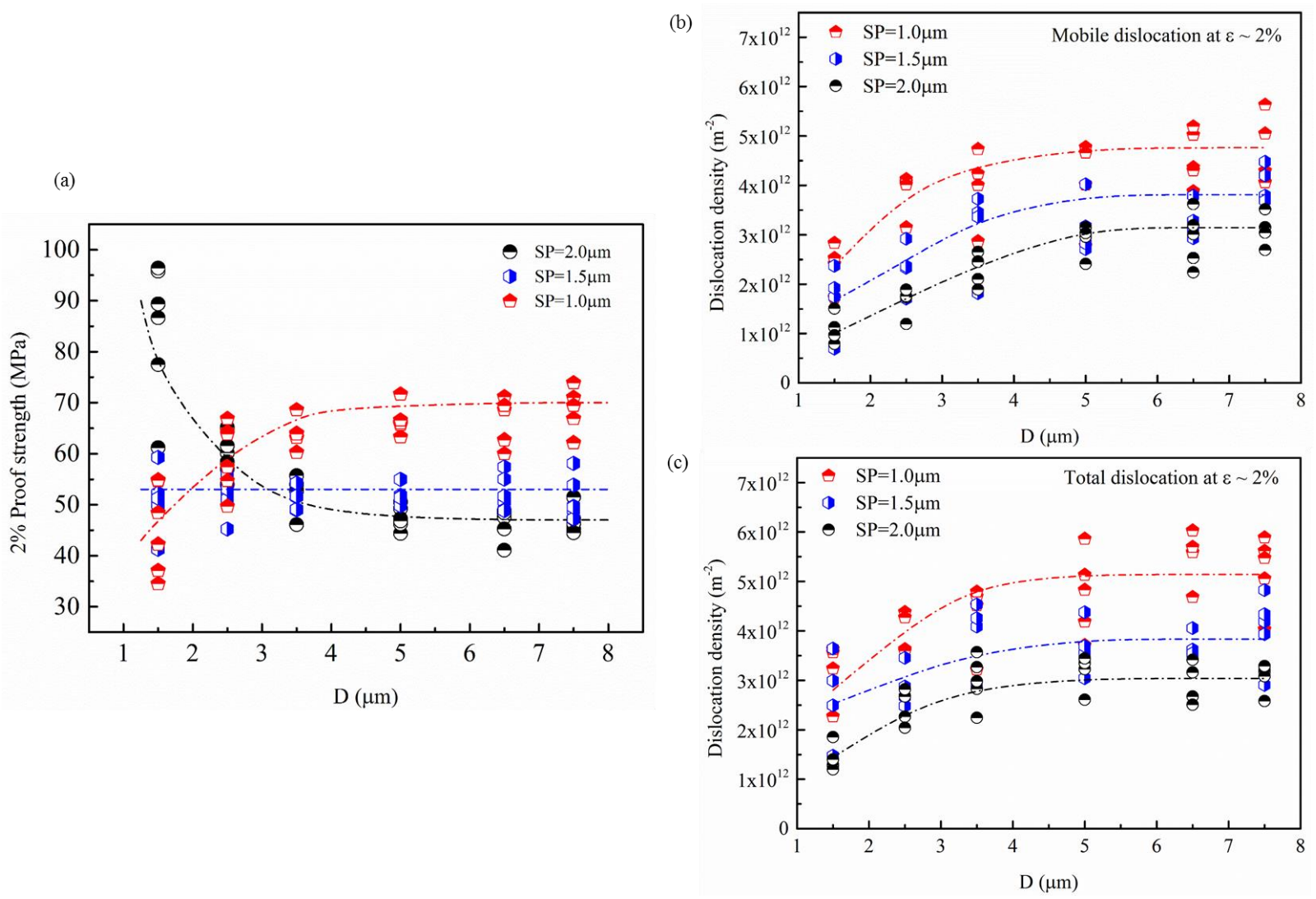

Figure 6. Results of 2D discrete dislocation dynamics simulations. (a) Predicted 2% proof strength of lamellar Sn/Pb micro-scaled specimens versus size *D* of simulation region with different lamellar spacing (SP). Predicted density of (b) mobile dislocations and (c) total residual dislocations in Sn/Pb micropillars with different SP at strain of ~2%.

Table 1. Material and modeling parameters used for eutectic Sn/Pb alloys

Parameters*	**Value**	
μ_1, μ_2[60]	18 GPa	5.6 GPa
E_1, E_2[60]	50 GPa	16 GPa
b_1, b_2 [55]	0.66 nm	0.35 nm
ΔG_1, ΔG_2 [54]	0.88 eV	0.79 eV
ν_1, ν_2	6.8×10^{12} Hz	4.3×10^{12} Hz
ω_1, ω_2	4.7/nm	2.5/nm
s_1, s_{2}**	~0.229	~0.206
n_1, n_2	0.85	0.675
C_1, C_2	0.047 $MPa^{-0.85}\cdot\mu m^{-2}$	0.045 $MPa^{-0.675}\cdot\mu m^{-2}$
m_1, m_2	2.45	2.05
k_{v1}, k_{v2}	2.25×10^{-4} $MPa^{-2.45}\cdot\mu m/s$	1.25×10^{-4} $MPa^{-2.05}\cdot\mu m/s$
k_{d1}, k_{d2}	34.75 $MPa\cdot\mu m^{-0.5}$	10.75 $MPa\cdot\mu m^{-0.5}$
$\dot{\sigma}$	2 MPa/s	
α	2.85 MPa· μm	
γ	0.0025	
k	~1.05	
h_{IPB}	~75 nm	
r	15.75	
θ	60°	

* Index 1 and 2 refer to Sn and Pb phase respectively. Parameters without references are observed from the present experiments or obtained by fitting the modeling prediction to experimental details.

** s_1 for the Sn phase was calculated from the observed micropillar axis of ~ [001], and s_2 for the Pb phase was estimated from the preferred crystallographic relationship of IPBs of $(1\bar{1}\bar{1})_{Pb} \parallel (011)_{Sn}$ and $[211]_{Pb} \parallel [211]_{Sn}$; see text for details.